Bio-Design and Manufacturing (2024) 7:1–13
https://doi.org/10.1007/s42242-023-00256-0

RESEARCH ARTICLE

Bionic lightweight design of limb leg units for hydraulic quadruped robots by additive manufacturing and topology optimization

Huaizhi Zong[1] · Junhui Zhang[1] · Lei Jiang[1,2] · Kun Zhang[1] · Jun Shen[1] · Zhenyu Lu[3] · Ke Wang[1] · Yanli Wang[4] · Bing Xu[1]

Received: 18 March 2023 / Accepted: 24 July 2023 / Published online: 9 December 2023

Abstract

Galloping cheetahs, climbing mountain goats, and load hauling horses all show desirable locomotion capability, which motivates the development of quadruped robots. Among various quadruped robots, hydraulically driven quadruped robots show great potential in unstructured environments due to their discrete landing positions and large payloads. As the most critical movement unit of a quadruped robot, the limb leg unit (LLU) directly affects movement speed and reliability, and requires a compact and lightweight design. Inspired by the dexterous skeleton–muscle systems of cheetahs and humans, this paper proposes a highly integrated bionic actuator system for a better dynamic performance of an LLU. We propose that a cylinder barrel with multiple element interfaces and internal smooth channels is realized using metal additive manufacturing, and hybrid lattice structures are introduced into the lightweight design of the piston rod. In addition, additive manufacturing and topology optimization are incorporated to reduce the redundant material of the structural parts of the LLU. The mechanical properties of the actuator system are verified by numerical simulation and experiments, and the power density of the actuators is far greater than that of cheetah muscle. The mass of the optimized LLU is reduced by 24.5%, and the optimized LLU shows better response time performance when given a step signal, and presents a good trajectory tracking ability with the increase in motion frequency.

Graphic abstract

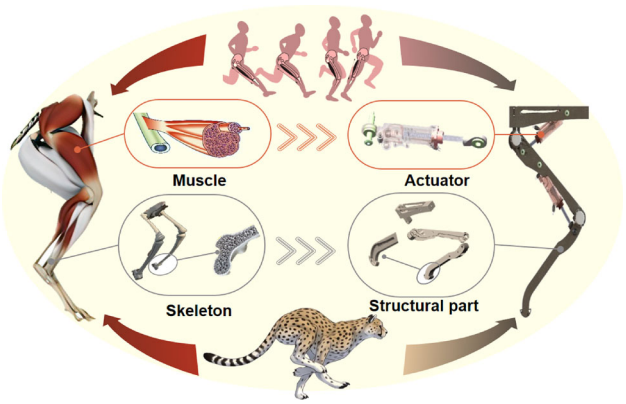

Keywords Additive manufacturing · Bionic lightweight design · Limb leg unit · Quadruped robot · Trajectory tracking

✉ Junhui Zhang
benzjh@zju.edu.cn

[1] The State Key Laboratory of Fluid Power and Mechatronic Systems, Zhejiang University, Hangzhou 310058, China

[2] Unmanned Vehicle Research and Development Center, China North Vehicle Research Institute, Beijing 100072, China

[3] School of Mechatronic Engineering, Nanchang University, Nanchang 330031, China

[4] Auclean High-Tech Ltd., Wuxi 214108, China

Introduction

Inspired by quadruped animals, especially cheetahs, many multi-legged robots have been recently developed. Compared to wheeled robots [1] or tracked robots [2], legged platforms demonstrate better flexibility and terrain adaptability due to their discrete ground support in rugged environments, such as mountains, jungle, or land covered in snow or ice. Quadruped robots are gaining popularity within robotics due to their superior gait stability and robustness to various disturbances. Taking inspiration from the cat family [3, 4], the urgent demand for high-speed and high-flexibility locomotion has prompted many robotics researchers to improve actuators, the mechanical design, and the control algorithms of quadruped robots. Superior to electrically driven quadruped robots, hydraulically driven quadruped robots such as the Wildcat [5] and HyQ [6] have been developed to achieve higher speeds and carry heavier payloads. However, closed-chain triangles consisting of a hydraulic linear cylinder and two connecting rods are complicated. To realize lightweight limb leg unit (LLU) designs, many researchers have focused on simplifying the leg structure and removing redundant mass.

To simplify the joint drive mechanism of the LLU, a centric slider–crank mechanism was introduced to the Wildcat. The lower leg served as the crank, and the knee joint actuator was embedded in the thigh as a slider, which avoided the frequent swing of the actuator. In addition, the leg mechanism was optimized, and the body weight of the Wildcat was thereby reduced. The Wildcat can reach a maximum speed of 32 km/h [5]. Moreover, Atlas, a bipedal humanoid robot with highly agile locomotion [7], adopted the same principle. With the use of three-dimensional (3D) printing and through the internal integration of multiple channels and the actuator into a single part, the weight of an Atlas robot was reduced from 152 to 80 kg. However, the rotary shaft seal is hard to guarantee under reciprocating actuation, and the built-in design can be challenging to manufacture and repair. In addition, rotary hydraulic cylinders can simplify the transmission mechanism of the LLU [8], which can output torque directly. In other examples, the HyQ-REAL robot from the Italian Institutes of Technology [9] and JINPOONG 1 from the Korea Institute of Industrial Technology [10] both used rotary cylinders as the actuators of hip joints, and the overall mechanistic complexity of the legs was thereby significantly reduced. However, rotary cylinders are relatively heavy and their low speed stability cannot be guaranteed due to excessive leakage on sealing contact surfaces. Hence, quadruped robots usually adopt closed-chain linkages with three hinges to provide rotating joint motion.

Aiming to reduce redundant mass, many efforts have been taken to propose a new actuator concept using lightweight structures. For instance, He and Gao [11] developed a novel hybrid actuator Hy-Mo that consisted of a low-friction cylinder, a novel valve driven by an electric motor, and two pressure sensors. This design eliminated the need for a cooler, filter, and accumulator, which realized a more compact and lightweight design, and featured lower leakage and better energy efficiency. Moreover, highly integrated hydraulic smart actuators share the same design as various other forms of processing technology [6]. Ultra-compactness can be achieved through the introduction of metal additive manufacturing, and external oil pipes and messy wire channels can be eliminated through internal integration. Xu et al. [12] put forward a new design in which a cylindrical barrel was replaced by local composite fiber reinforced polymers (CFRP). This reduced the mass of hydraulic linear cylinders by 40%. Considering the complex sealing system and sliding surface for the piston seal, the barrel used a processed aluminum alloy as a liner, and fibers were wound on it after dipped in liquid resin. In addition, some scholars have paid attention to the lightweight design of this mechanical structure. For example, researchers from ETH Zürich [13] unlocked the potential involved in redesigning and developing the lower leg of a hydraulically actuated quadruped robot by combining CFRP with additive manufacturing. In this design, the leg was separated into four parts, each manufactured using different processes, including additive manufacturing, filament winding, and fused deposition modeling. In addition, topology optimization can be effective for minimizing structural weight and guaranteeing a certain level of performance [14], which is why it is widely applied [15, 16]. At present, topology optimization has also been applied to hydraulic quadruped robots. Huang et al. [17] presented one approach to removing excessive hydraulic cylinder end cap volume through additive manufacturing and topology optimization. This process took both optimal geometries and flow channels into consideration, and the volume of the end cap was reduced by 50.7%. Although most cases have shown satisfying results in mass reduction, the optimization effect using the methods described above is local, not global. Furthermore, designing and manufacturing a lighter LLU within a strength constraint, as well as quantitatively analyzing the relationship between weight reduction and movement speed, had rarely been performed.

Inspired by the skeletal muscles and leg structures of cheetahs, this paper presents a custom, highly integrated hydraulic skeletal muscle-like actuator and optimized structural parts adopting the bionic design concept to solve these problems. Here, the cylinder barrel was designed with integrated flow paths using additive manufacturing, and exhibits a very compact design. In addition, hybrid lattice structures were introduced to reduce the weight of the piston rod. Topology optimization was used to remove the extra material from the structural parts. These three newly designed components (hip part, thigh part, and lower leg) were all additively

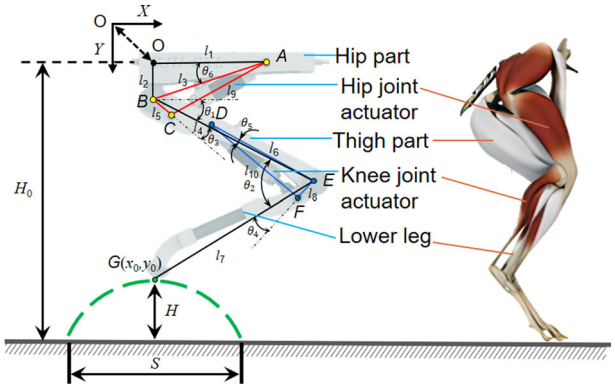

Fig. 1 Simplified model of LLU based on the cheetah skeleton–muscle system. LLU: limb leg unit

manufactured using $AlSi_{10}Mg$. Finally, the dynamic performance enhancement of the proposed LLU was analyzed quantitatively using step response and trajectory tracking experiments.

This paper is constructed as follows. Sect. "Analysis and performance requirements of the LLU" describes the overall design of the LLU and its performance requirements. The bionic lightweight design of the LLU is introduced in two aspects: the hydraulic actuator design (Sect. "Highly integrated hydraulic cylinder design") and structural part topology optimization (Sect. "Topological optimization of structural parts"). Then, the experimental results are expressed in Sect. "Results and discussion", followed by a conclusion in Sect. "Conclusions."

Analysis and performance requirements of the LLU

Overall design

The two-degree-of-freedom LLU depicted in Fig. 1 consists of hip and knee joints, which are represented by B and E, respectively. A and C indicate the connecting positions of the hip joint actuator with the hip and thigh parts, respectively. D and F indicate the connecting positions of the knee joint actuator with the thigh and lower leg parts, respectively. G indicates the touching point at the foot end to O.

The complex mechanical structure of the LLU is simplified (Fig. 1) for the convenience of modeling and analysis. Here, we use l_1 and l_2 as the lengths of OA and OB, respectively. l_3 and l_5 represent the mechanical parameters of the hip joint, AB and BC, respectively. l_6 and l_8 represent the mechanical parameters of the knee joint, DE and EF, respectively. l_4 and l_7 denote the lengths of the thigh part and the lower leg, respectively. In Fig. 1, ΔABC and ΔDEF are the driving triangles of the hip joint and the knee joint, respectively. The kinematic dimensions of each link are given in Table 1. The origin of the coordinate frame O is set at the hip part. H_0 indicates the distance along the vertical axis from the foot end to O.

Performance requirements

Many quadruped robot prototypes have been developed and demonstrated a variety of motions including squatting, walking, and trotting [18, 19]. However, many problems have appeared during debugging and maintenance, including distributed oil pipes that interfere with the movement of the LLU and leakage due to excessive oil interfaces. To realize a higher motion velocity of the LLU, we first developed a list of technical requirements:

1. achieving a compact design and fewer connections by adopting new manufacturing processes;
2. developing a layout for the oil pipes to offer sufficient workspace for the swing motion of the LLU;
3. integrating the design of the actuators and servo valves for the high-performance control of the LLU;
4. introducing a lightweight design of the actuators and structural parts to reduce the overall mass of the LLU.

Regarding lightweight design principles, based on the biomechanical studies of animals of different sizes [20], stride frequency is known to be related to mass. This is represented by the following equation:

$$f = 3.35 \times M_0^{-0.13}, \tag{1}$$

where f is the stride frequency at the preferred trotting speed, and M_0 is the mass of the animal.

The preferred stride frequency for a trotting gait can therefore be obtained as follows:

$$f = 3.35 \times (m_{\text{torso}} + 4 \times m_{\text{leg}})^{-0.13}, \tag{2}$$

where m_{torso} is the mass of the torso and m_{leg} is the mass of the leg.

Equation (2) reveals that the stride frequency increases when the mass of the LLU reduces. This quantitative relationship can be taken as the key optimization design principle of the LLU.

Highly integrated hydraulic cylinder design

Muscles generate mechanical force according to stimulation by motor neurons, and the energy required for muscle contraction is carried through the blood [21]. These effect and

energy transmission modes are similar for hydraulic cylinders; i.e., after receiving a signal from a control unit, a piston rod extends or retracts, as shown in Fig. 2. With these structural characteristics, a bionic hydraulic actuator needs to be designed to achieve the dual functions of weight reduction and the integration of its core components, including a cylinder barrel with an embedded flow path, a piston rod, and other accessory elements.

Cylinder barrel design

The cylinder barrel is chiefly used as connection interfaces for multiple parts, and includes a rotary direct drive servo valve, a hinged end, two pressure sensors, and external flow channels. Here, additive manufacturing is introduced to realize integration design, and the model of the cylinder barrel we developed is shown in Fig. 3a. Here, the oil inlet and outlet are arranged on the same side, which are connected to the rod-side and piston-side cavities through embedded flow channels. Two pressure sensors are, respectively, connected to the rod-side and piston-side chambers to estimate the transient force. This can help to achieve contact force control and avoid impact failure when the foot end is in contact with the ground; this results in higher reliability and less signal noise. The servo valve is installed on the valve block on the top of the cylinder barrel by four threads.

The integrated design method is inspired by blood vessels and reduces the steps involved in oil movement, resulting in a smoother transition for oil flow, and thereby improving performance and avoiding energy dissipation. In addition, the envelope dimensions of the actuator are minimized, and the total weight is lower. According to the working conditions of the LLU, the stress analysis of the cylinder barrel is shown in Fig. 3b. An internal pressure of 21 MPa is applied on the cylinder barrel and the embedded hydraulic pipes, the hinged end is subject to an axial force of 10,000 N, and a fixed constraint is set on the right outer ring of the barrel. The static simulation results are shown in Fig. 3c, with a maximum stress of 222.97 MPa that does not exceed the allowable stress.

Piston rod design

As the core component of the actuator, the outer diameter of the piston rod is usually small. In addition, to guarantee the seal between the cylinder barrel and the piston rod, the piston rod usually offers interfaces for a Glyd ring and a guide ring, and therefore this shape may not be a standard stepped shaft. As the element that transfers output force, the compression of the load affects the reliability and fatigue strength, as well as the stability of the compressed piston rod. In addition, it should resist the impulsive force when the foot touches the ground. Complicated force conditions

Table 1 Mechanical structure parameters of the limb leg unit

Parameter	l_1	l_2	l_3, l_6	l_4, l_7	l_5, l_8
Link length (mm)	216.22	72.30	228.00	350.00	45.00

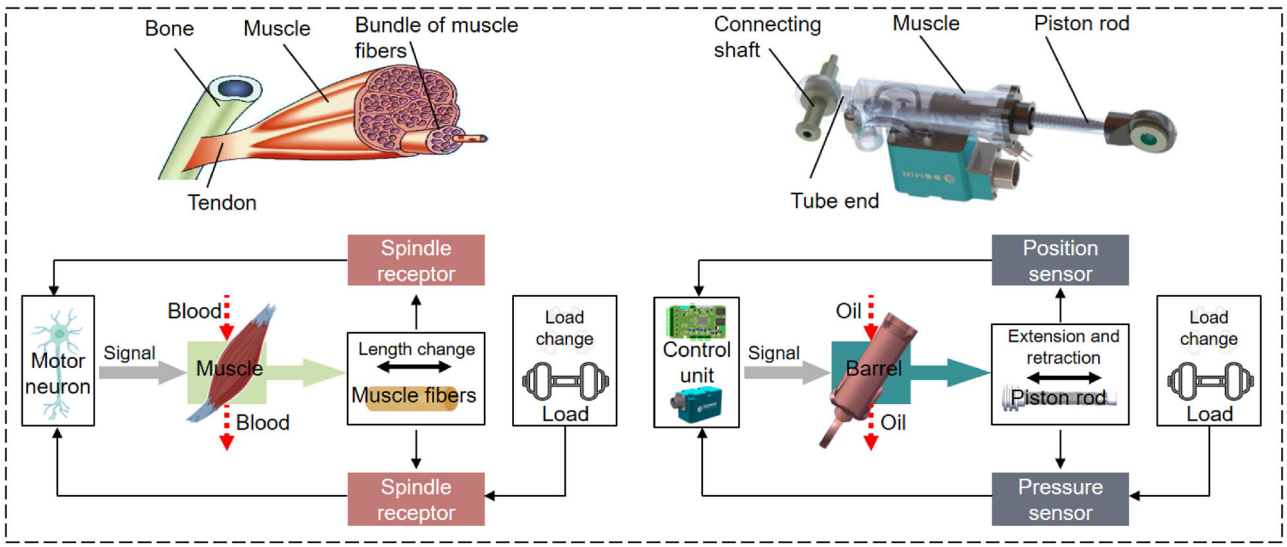

Fig. 2 Biomimetic design of a hydraulic actuator

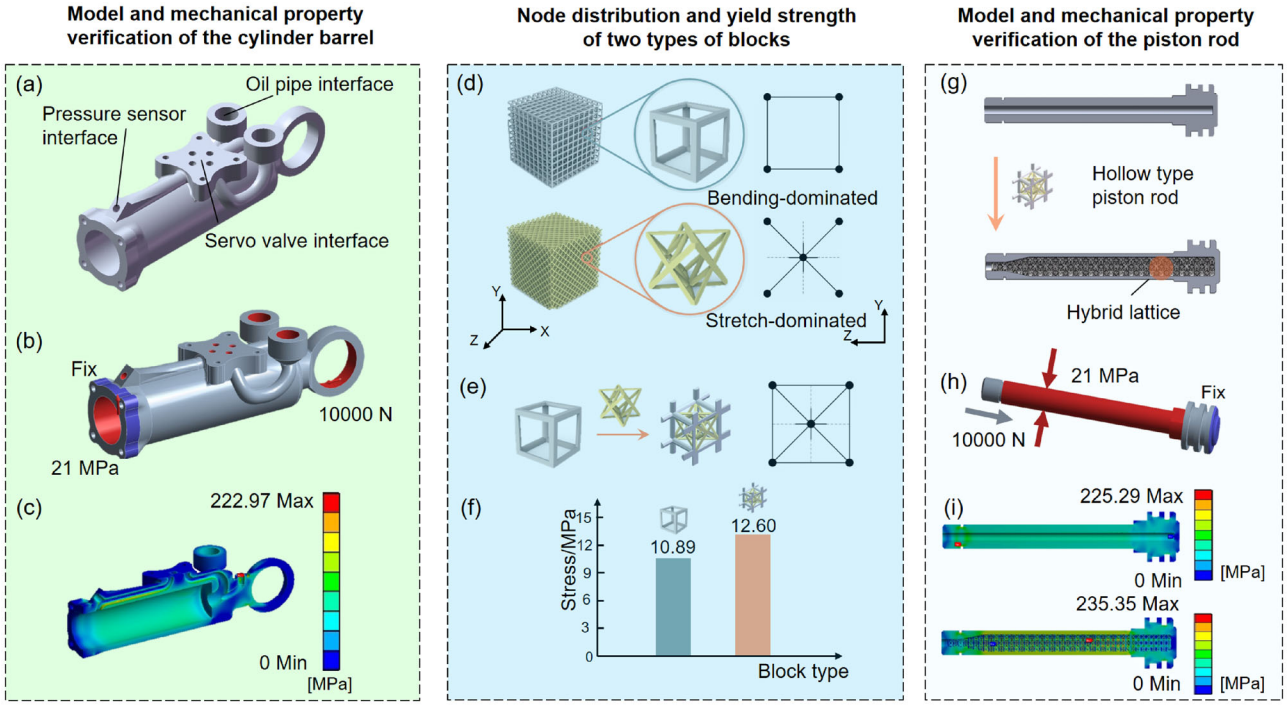

Fig. 3 Model and mechanical property verification of the cylinder barrel and piston rod: **a** cylinder barrel model, **b** stress analysis of the cylinder barrel, **c** finite element simulation results of the cylinder barrel, **d** single unit blocks, **e** hybrid unit block, **f** yield strength at 0.1 volume ratio, **g** piston rod model, **h** stress analysis of the piston rod, and **i** finite element simulation results of the piston rod

and a confined envelope size can hinder the development of lightweight piston rod designs.

Lattice structures are 3D arrangements of many smaller units, and their mechanical properties can be easily manipulated by adjusting the unit type or spatial layout. Therefore, the piston rod can be lightened without changing the dimension. Moreover, since the compression performance, bending performance and energy absorption cannot be simultaneously satisfied by a type of lattice structure, a hybrid lattice concept is proposed to integrate the advantages of two or more kinds of lattice structures.

Here, we refer to previous studies published by our group regarding the mechanical properties of different lattice types [22], especially a bending-dominated unit called "Grid" and a stretch-dominated unit named "Octet." These units, depicted in Fig. 3d, are combined according to a tensile modulus peak value, as shown in Fig. 3e. Figure 3f illustrates that the yield stress increases by 15.7% after adding the Octet block to the Grid block.

A sectional view of the piston rod is shown in Fig. 3g in which most of the piston rod structures that were originally solid are replaced with hybrid lattices. The weight of the piston rod is thereby reduced by 23% relative to a hollow piston rod. Moreover, for removal of residual powder effectively, an opening hole is reserved.

The hybrid design method applied to the piston rod finds the best compromise for achieving a lightweight design with adequate durability and performance within limited available space. A simulation force setting of the piston rod is shown in Fig. 3h. Here, an external pressure of 21 MPa is added to the piston rod, and it is then subjected to an axial force of 10,000 N with the right end face fixed. The static simulation results for the two types of piston rod are shown in Fig. 3i, and they show maximum stresses of 225.29 and 235.35 MPa, respectively. Although the maximum stress increased slightly, the average stress of the piston rod reduced by 15.3% from 63.09 to 53.45 MPa relative to the original design.

Manufacturing and operational testing of the actuator

First, the cylinder barrel and the piston rod were additively manufactured using a selective laser melting machine (Huffman Corporation, United States, HP-115CL) with $AlSi_{10}Mg$ aluminum alloy powder. A focused laser beam of 500 W was deflected to solidify the metal powder, and the spot size was set to 80.00 μm. The layer thickness during manufacturing was 30.00 μm, and the scan speed was 1200 mm/s.

Next, post-processing techniques, including machining, heat treating, and finishing, were used to remove residual powder and reserved layers from the metallic work pieces,

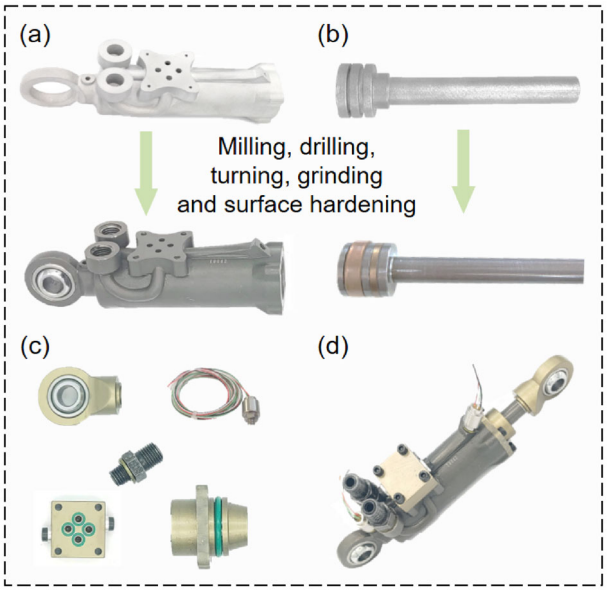

Fig. 4 Manufacturing of the actuator: **a** cylinder barrel, **b** piston rod, **c** accessory components, and **d** highly integrated hydraulic actuator

as shown in Figs. 4a and 4b. The Glyd ring mounted on the piston acts as a pressure barrier between the two chambers. Then, two guide rings were installed to absorb radial loads and ensure that the piston and piston rod are centered within the cylinder barrel. The end cap is usually attached to the cylinder barrel using a threaded connection, which contains the entire sealing system for the piston rod. A step seal was used to prevent the working fluid from leaking, and a wiper seal was used to prevent dust, debris, and moisture from entering the cylinder, as depicted in Fig. 4c. The completed integrated hydraulic actuator is shown in Fig. 4d.

Site acceptance tests showed that the actuators complied with the demands of the optimized design. After 10,000 extension and retraction motions, the actuators showed no signs of internal or external leakage, and the starting pressure of the integrated actuators was 0.18 MPa. In addition, the initial length and stroke of the actuators remained the same as those of the original actuator.

Topological optimization of structural parts

The original structural parts were manufactured by direct milling and drilling of metal. Using conventional manufacturing methods results in the inclusion of many unnecessary volumes that account for a large proportion of the structural parts weight. Many studies have shown that bone structures, such as those found in the human body, can be taken as examples of good reference designs with respect to shape, size, and orientation [23, 24]. Moreover, the hollow structure enhances the bending resistance of bone without making bones heavy. Thus, inspired by the structures of the skeleton shown in Fig. 5a, hollow structures with dense structures at both ends have been created for use in the original LLU. However, there still exists redundant mass, and topology optimization was introduced to remove the material in the least loaded areas.

Topology optimization model

Topology optimization is a mathematical method that optimizes material layout within a given design space and a given set of loads via different algorithms. Of these algorithms, the solid isotropic material with penalization algorithm for topology optimization penalizes intermediate densities to encourage discrete void-solid designs, and therefore caters to the mass reduction demand of the structural parts of LLU as shown in Fig. 5b.

A topology optimization model designed to minimize structural strain energy with volume constraints can be described as follows:

$$\begin{cases} \min \quad C(\boldsymbol{x}) = \dfrac{1}{2}\boldsymbol{u}^{\mathrm{T}}\boldsymbol{K}\boldsymbol{u} = \dfrac{1}{2}\displaystyle\sum_{i=1}^{n}(x_i)^P \boldsymbol{u}_i^{\mathrm{T}}\boldsymbol{K}_0\boldsymbol{u}_i, \\ \text{subject to } \boldsymbol{K}(\boldsymbol{x})\cdot\boldsymbol{u}(\boldsymbol{x}) = \boldsymbol{F}, \\ \dfrac{V(\boldsymbol{x})}{V_0} = \text{volfrac}, \\ 0 < x_{i\min} \le x_i \le x_{i\max} \le 1, \end{cases} \tag{3}$$

where $\boldsymbol{x}=(x_1, x_2, ..., x_n)^{\mathrm{T}}$ is the cell density vector, and $x_{i\min}$ and $x_{i\max}$ are the lower and upper limits of x_i, respectively; $C(\boldsymbol{x})$ is the flexibility of the structural parts; $\boldsymbol{u}$ is the total displacement vector and $\boldsymbol{u}_i$ is the unit displacement vector; $\boldsymbol{K}$ is the stiffness matrix and $\boldsymbol{K}_0$ is the initial cell stiffness matrix; $\boldsymbol{F}$ is the loading matrix; P is the penalty factor; V is the volume fraction and V_0 is the initial volume fraction; volfrac denotes the given volume fraction.

Topology optimization process

A force analysis of LLU is shown in Fig. 5c. Here, two actuators are simplified as rigid mechanical linkages to transfer a force of 1500 N exerted on the foot end. Importantly, the hip structure is fixed throughout this simulation. The finite element analysis results shown in Fig. 5d are then taken as inputs for topology optimization. Taking minimum compliance as the objective, the penalty factor was set to three [25], and the response constraint condition was set to the volume percentage in which the volume retained percentages were 90% for the hip part and 50% for the other parts.

The optimization processes for the structural components of the LLU are illustrated in Fig. 5e. Here, the optimal material distributions were derived by increasing or decreasing the materials used. Because the optimization mass range was

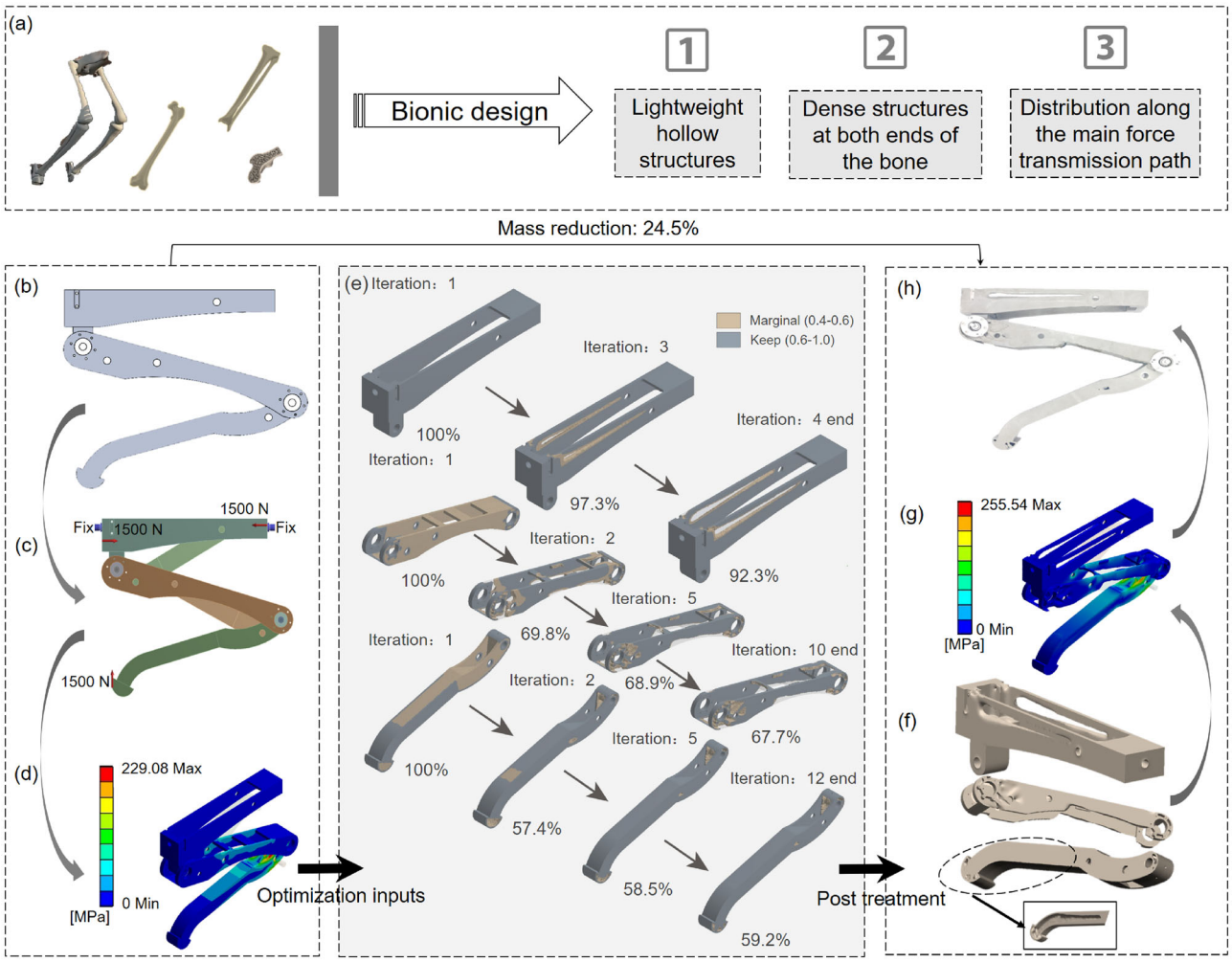

Fig. 5 Optimization procedure for LLU structural components: **a** characteristics of bone structures, **b** original model, **c** schematic diagram of force direction, **d** finite element simulation results before optimization, **e** process of topology optimization, **f** structural parts prototype,**g** finite element simulation results after optimization, and **h** model after topology optimization. LLU: limb leg unit

only 10%, the optimization of the hip joint was completed after four iterations. According to these topology results, the hip and thigh parts showed material reduction on the side, and the lower leg was hollowed out to include a cavity within the structure. The smoothed element models after manual removal of the burr are shown in Fig. 5f. Moreover, finite element analysis results of the LLU are shown in Fig. 5g. These results show that the maximum stress is 255.54 MPa within the allowable stress of $AlSi_{10}Mg$. Finally, the rationality of the optimized model is demonstrated in Fig. 5h.

Results and discussion

Weight reduction

The original LLU, shown in Fig. 6a, consists of CFRP actuators, structural components manufactured by milling or drilling processes, a rubber buffer, and connectors. The geometry of the LLU has been shown to be reasonable based on plots of the maximum hydraulic actuator torque versus the joint angle for extending and retracting cylindrical motion. Hence, the length of the structural parts and the parameters of the two actuators remain unchanged during the optimization processes. Moreover, the optimized LLU is shown in Fig. 6b, and includes two highly integrated actuators with rotary direct drive valves and new structural components designed using topology optimization.

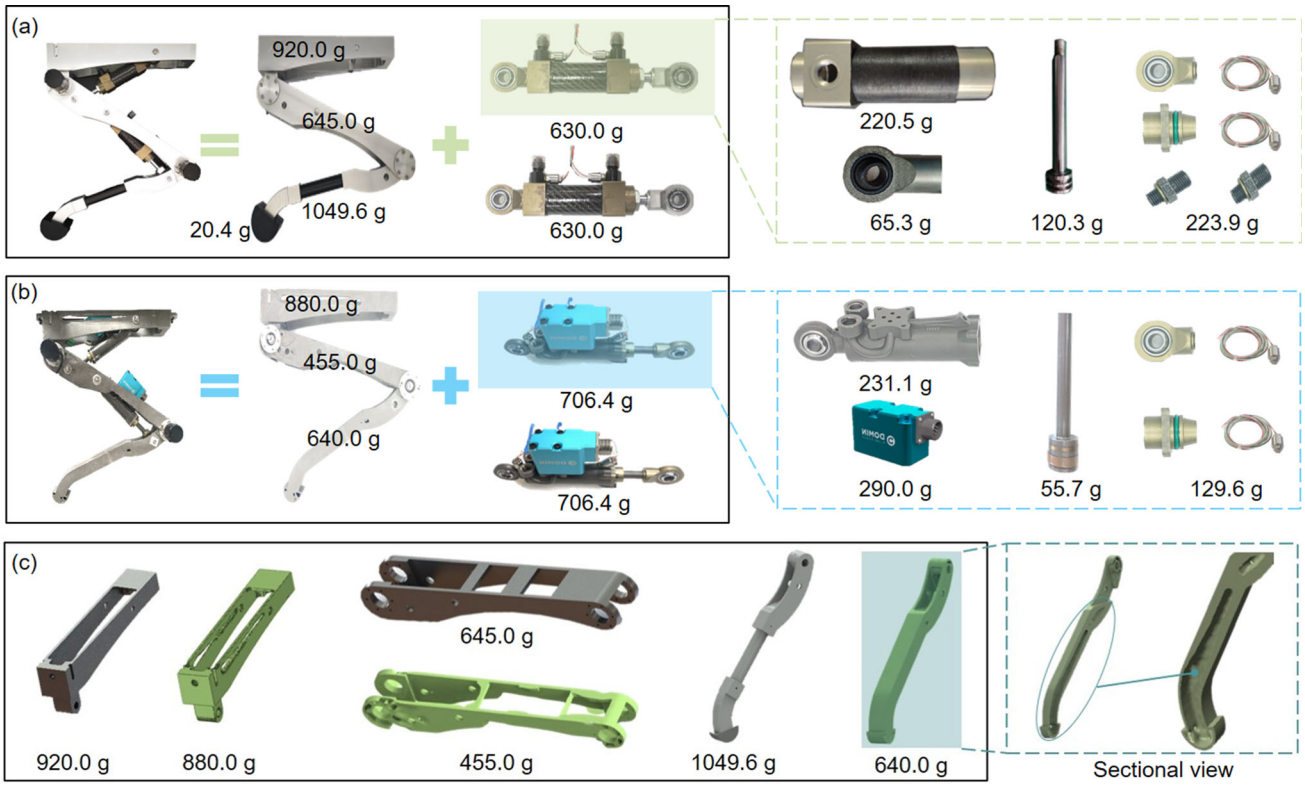

Fig. 6 LLU prototype before and after optimization: **a** mass distribution and components of the original LLU, **b** mass distribution and components of the optimized LLU, and **c** weight reduction of the three structural parts. LLU: limb leg unit

The mass of the additively manufactured hydraulic cylinder is 416.4 g, representing a reduction of 33.9% relative to the CFRP hydraulic cylinder. In addition, the mass of the highly integrated barrel is 231.1 g, representing a reduction of 19.1% compared to the CFRP barrel including the end cap. This reduction is achieved despite the fact that the CFRP barrel itself had already been lightened significantly relative to the barrels of mature industrial actuators. More than half of the piston rod weight was reduced through adoption of hybrid lattice structures, and fewer accessories were used after optimization.

Table 2 shows the weight reduction of the optimized LLU after the introduction of metal additive manufacturing and topology optimization. Weight reduction was realized in various degrees in three structural parts of the LLU. As shown in Fig. 6c, the weight of the hip part was reduced by 4.3% via removal of excess material. The weight reduction of the thigh part reached 29.5%, with most of the weight reduction concentrating at the left and upper ends. The lower leg yielded the most significant mass reduction by exchanging solid metal with cavity, and the wall thickness was gradually decreased toward the foot end, which resulted in a weight reduction of nearly 409.6 g. The mass of the set of structural components was reduced by 24.5%, and the total mass of the LLU decreased from 4970.0 to 4090.0 g, representing a reduction of 17.7%. Notably, the lightweight design of the LLU has a positive effect on the whole quadruped robot, since it decreases the demand on the hydraulic power unit and further lightens the mass of the robot torso. In addition, the manifold and other connection components can be optimized by further adoption of the metal additive manufacturing process.

Table 2 Weight reduction after lightweight design

Configuration/component	Original weight (g)	Optimized weight (g)	Weight reduction (%)
Hip part	920.0	880.0	4.3
Thigh part	645.0	455.0	29.5
Lower leg	1049.6	640.0	39.0
Actuator (without valve)	630.0	416.4	33.9
Limb leg unit	4970.0	4090.0	17.7

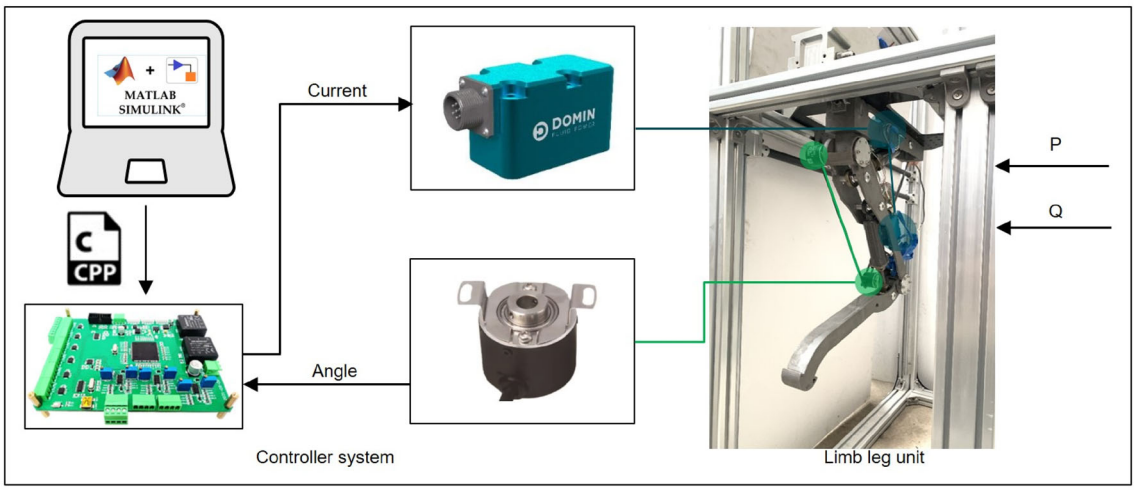

Fig. 7 Experimental setup for performance tests

Bench tests

Figure 7 depicts the experimental setup used to assess the dynamic performance versus mass reduction relationship of the LLU prototype. In addition, Table 3 shows the detailed parameters of the bench test. The LLU control framework was built using MATLAB/SIMULINK and was converted into C language using Code Composer Studio environment. The hypogynous machine was comprised of a digital signal processor TMS320F28335 controller with other chips. This controller can receive instruction signal through a controller area network (CAN) bus. Given the excellent performance of DOMIN S4 PRO servo valves in the consistency and frequency response, the extension and retraction of two actuators were implemented with two DOMIN S4 PRO servo valves. Two absolute angle encoders, OIDC3815S24S, were installed at the rotating shaft to measure the position of the hip and knee joints.

Step response experiments and trajectory tracking experiments were implemented to evaluate the dynamic performance improvement of the optimized LLU. All experiments were developed under the same pressure of 14 MPa, and a closed-loop proportion integration differentiation (PID) controller was adopted for all joints. A whole block diagram of the control algorithm is depicted in Fig. 8. Notably, during the tests of the original and optimized LLUs, two DOMIN S4 PRO servo valves were applied to control the joint actuators to ensure experimental accuracy.

LLU step response experiments

The step response experiments of the foot end of the LLU were developed to evaluate the performance improvement after the optimization of the actuator and the structural components. For these tests, a 200 mm step signal was introduced in four different conditions as shown in Fig. 9a; these included horizontal abduction/adduction and vertical abduction/adduction.

Figure 10 shows that the speed improvements of the foot end were visibly noticeable in all four cases. This result reveals that the mass reduction was conductive to higher motion speed of the LLU. Of the four motion directions, the maximum speed increase occurred for vertical adduction,

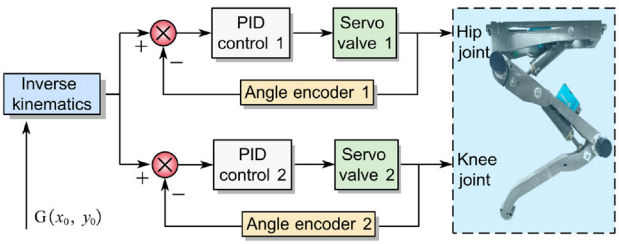

Fig. 8 Block diagram of the control algorithm during the performance tests

Table 3 Parameters of the bench test

Item	Value
Working pressure	14 MPa
Hydraulic oil	46#
Step response of valves at 100% step rate	<3.0 ms
Frequency response (±25% signal)	>150 Hz
Inner diameter of cylinder barrel	25.0 mm
Diameter of piston rod	12.0 mm
Actuator stroke	72.0 mm

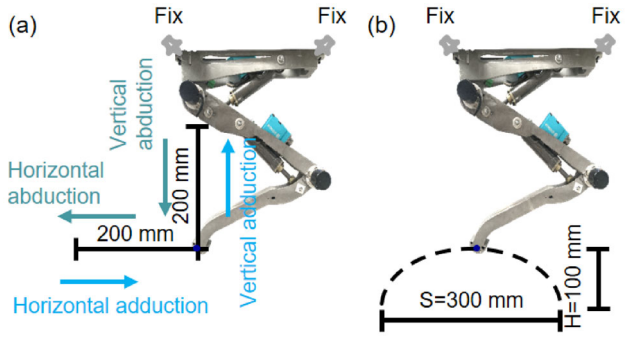

Fig. 9 Schematic diagram of motion trajectory: **a** schematic diagram of step response at foot end, **b** foot trajectory

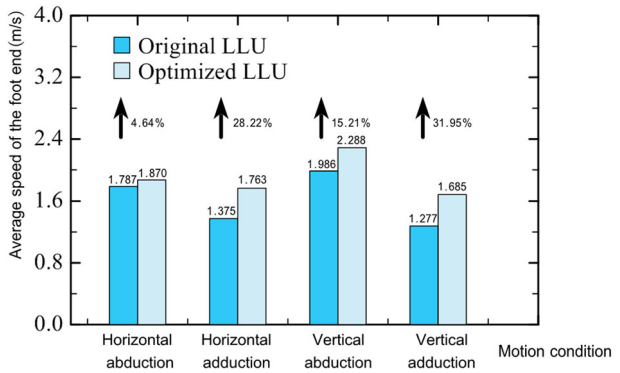

Fig. 10 Average speed of the foot end step response before and after optimization

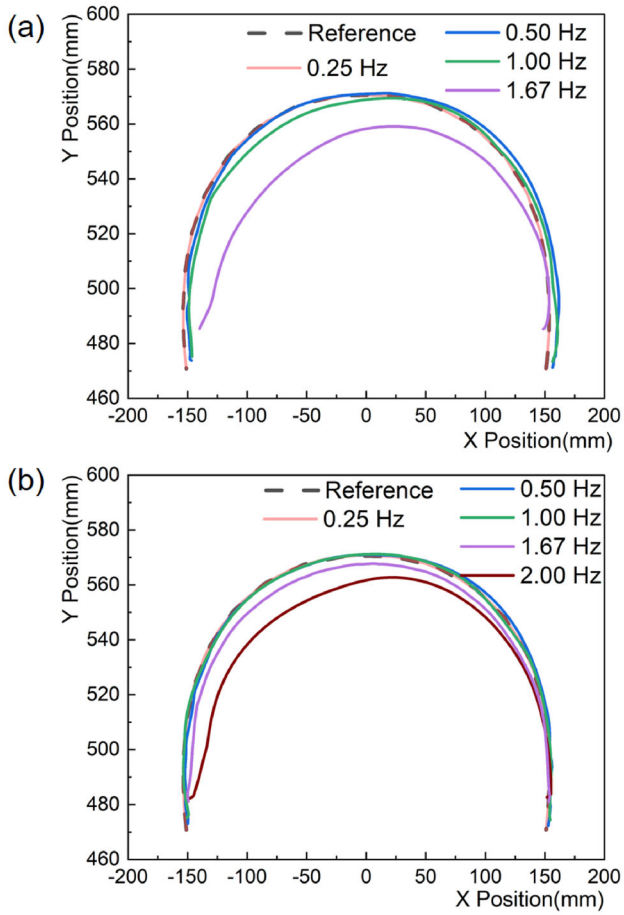

Fig. 11 Foot position trajectories of the air-walking motion at different movement frequencies: **a** original LLU, **b** optimized LLU. LLU: limb leg unit

with an increase of 31.95%. This was followed by the horizontal adduction motion direction, which saw an increase in the speed of the foot end from 1.375 to 1.763 m/s, representing an increase of 28.22%. The speeds of the vertical abduction of the two LLUs were 1.986 and 2.288 m/s, respectively. The smallest increase in speed was for the horizontal abduction direction, which increased slightly from 1.787 to 1.870 m/s.

Notably, when the direction of the motion was adduction, the lightweight LLU showed a more obvious speed increase. This was due to the fact that in this direction, the LLU moved opposite gravity, and weight was therefore more significantly involved in these movements.

Trajectory tracking experiments

A quintic polynomial trajectory model was adopted for the foot end as shown in Fig. 9b. The duty cycle of the gait β was 0.5, and the step length S was 0.3 m. The stride H was 0.1 m, and the initial height of the LLU H_0 was 0.55 m. The equations for the foot trajectory are as follows:

$$x(t) = \begin{cases} 0.3\left(6t^5 - 15t^4 + 10t^3\right) - 0.5S,\ 0 < t \le 0.5, \\ 0.3\left(6(1-t)^5 - 15(1-t)^4 + 10(1-t)^3\right) - 0.5S,\ 0.5 < t \le 1, \end{cases} \tag{4}$$

$$y(t) = \begin{cases} 0.55 - 0.1\left(6t^5 - 15t^4 + 10t^3\right),\ 0 < t \le 0.25, \\ 0.55 - 0.1\left(6(0.5-t)^5 - 15(0.5-t)^4 + 10(0.5-t)^3\right),\ 0.25 \le t \le 0.5, \\ 0.55 - 0.1\left(6(t-0.5)^5 - 15(t-0.5)^4 + 10(t-0.5)^3\right),\ 0.5 \le t \le 0.75, \\ 0.55 - 0.1\left(6(1-t)^5 - 15(1-t)^4 + 10(1-t)^3\right),\ 0.75 \le t \le 1. \end{cases} \tag{5}$$

Figure 11 shows the foot position trajectory for the air-walking motion task. Here, it can be observed that the experimental trajectories of the two LLUs were in perfect agreement with the given trajectories when the foot movement frequency was 0.25 Hz. However, with increasing motion frequency, the foot end of both LLUs gradually deviated from the target point, and the tracking effect of the

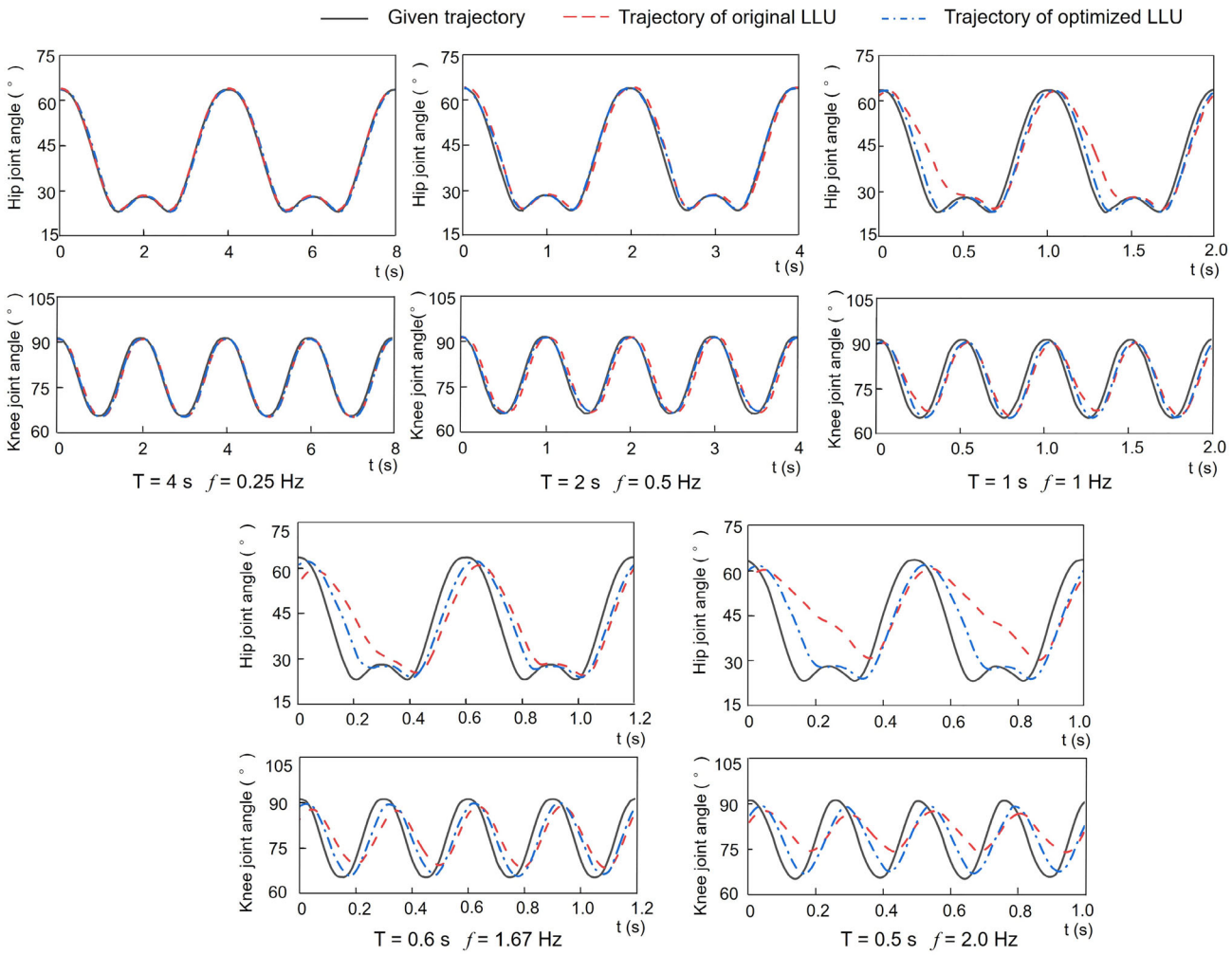

Fig. 12 Joint angle changes at different motion frequencies

original LLU was worse than that of the optimized LLU at the same frequencies.

When the foot end tracked the given trajectory, the angles of the two joints at different motion frequencies were measured to evaluate the tracking effect. These results are shown in Fig. 12, and the experimental results followed well with the given signals for both the hip and knee joints when the motion frequency was lower than 0.25 Hz. However, as the motion frequency increased from 0.25 to 1.0 Hz, tracking errors in amplitude and phase trended slightly upward. When the frequency reached 1.67 Hz, the original LLU was unable to follow the preset trajectory due to its weight limit being reached. In contrast, the optimized LLU tracked better than the original LLU, although the amplitude and phase were not satisfying.

The joint angle errors of the two LLUs are shown in Fig. 13. For example, the hip joint of the original LLU showed an average tracking error of 1.02° at 0.25 Hz, 2.04° at 0.5 Hz, 4.11° at 1.0 Hz, and 7.05° at 1.67 Hz. For the knee joint, the average tracking error was 0.92° at 0.25 Hz, 2.27° at 0.5 Hz, 3.74° at 1.0 Hz, and 4.30° at 1.67 Hz. Thus, both joints showed increased errors at higher frequencies. Specifically, an obvious error increase was seen after the frequency exceeded 1.67 Hz. Furthermore, at the 2.0 Hz condition, the average tracking error was 12.93° for the hip joint and 10.54° for the knee joint. Finally, the maximum error was 26.73° for the hip joint and 21.07° for the knee joint.

With respect to the optimized LLU, the average tracking error of the hip joint was 0.83° at 0.25 Hz, 1.89° at 0.5 Hz, 3.94° at 1.0 Hz, and 5.46° at 1.67 Hz. The average tracking error of the knee joint was 0.78° at 0.25 Hz, 1.87° at 0.5 Hz, 2.56° at 1.0 Hz, and 4.00° at 1.67 Hz. The same upward trend continued to 2.0 Hz, where the average tracking error was 6.68° for the hip joint, and 7.53° for the knee joint.

These results show that the joint angle errors of the optimized LLU at different frequencies were less than those of the original LLU, and the average error in the hip joint was

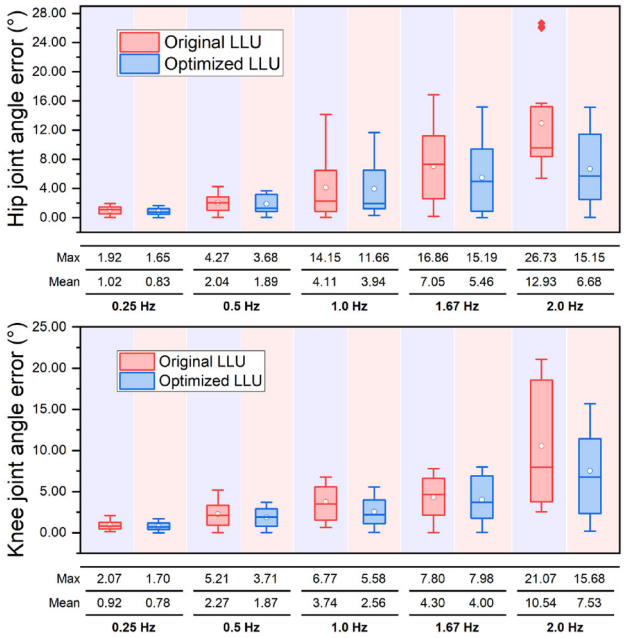

Fig. 13 Joint angle errors at different motion frequencies

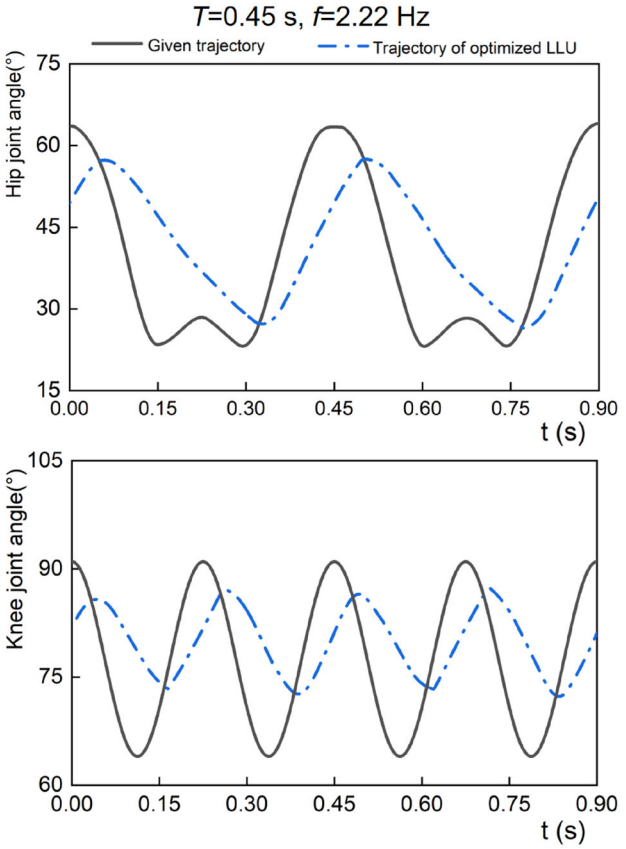

Fig. 14 Angle changes of two joints during the 2.22 Hz motion condition

reduced by 22.55% at 1.67 Hz. In addition, higher motion frequency values were reached after optimization, as evidenced by the foot tracking data depicted in Fig. 11 and the growth in tracking error shown in Fig. 13.

In addition to the average speed and the tracking error, we examined the tracking effect versus motion frequency to evaluate the performance improvement of the optimized LLU. According to Fig. 11 and the tracking results at 2.22 Hz shown in Fig. 14, it can be seen that in contrast to the tracking performance of the original LLU at 1.67 Hz, the optimized LLU reached the same limit at 2.22 Hz. Thus, higher motion frequencies can be realized with the same tracking effect, and the frequency increased by 32.93% after optimization of the actuator and structural components. Moreover, with the same step length (0.3 m) and limit motion frequency (1.67 Hz, 2.22 Hz), the maximum speed of the foot end increased from 1.00 to 1.33 m/s after optimization.

Conclusions

Inspired by the skeleton–muscle system of cheetahs and humans, this paper presented a novel bionic optimization approach for the LLUs of quadruped robots. The optimal LLU contained two highly integrated actuators and new structural components designed via topology optimization. The mechanical properties and dynamic performance enhancement were then verified by finite element analysis and prototype experimentation. The main conclusions are summarized as follows.

- Strengthening the piston rod using hybrid lattice structures achieved better mechanical properties with less metal materials, and helped to create a lightweight piston rod design. Moreover, modeled after the blood vessels within muscles, the cylinder barrel was embedded with many interfaces for two pressure sensors and many internal flow paths. This enabled it to realize excellent compactness with the aid of metal additive manufacturing. Consequently, the actuator had a reasonable layout and avoided motion interference and leakage.
- A considerable weight reduction effect was validated following topology optimization of the LLU. The material distribution results were similar to bone structures. The mass of the structural parts was reduced by 24.5% with similar linkages.
- The performance enhancement of the optimized LLU was described quantitatively via step response and trajectory tracking experiments.

Future work will concentrate on tapping the potential of additive manufacturing to realize an ultra-lightweight mechanism. Moreover, the advantages of introducing hybrid lattice structures will be analyzed in greater detail in the future. Finally, the derivation of more precise dynamic models

may contribute to ultra-lightweight designs, and such performance enhancements can be validated on a quadruped robot.

Acknowledgements The work is supported by the National Natural Science Foundation of China (Nos. U21A20124 and 52205059) and the Key Research and Development Program of Zhejiang Province (No. 2022C01039).

Author contributions Conceptualization contributed by HZZ and JHZ; methodology contributed by HZZ, LJ, and KZ; resources contributed by HZZ, KW, and YLW; validation contributed by HZZ and ZYL; writing—original draft contributed by HZZ; writing—review and editing contributed by HZZ and JS; supervision contributed by JHZ; funding acquisition contributed by JHZ, ZYL, and BX. All authors have read and agreed to the published version of the manuscript.

Declarations

Conflict of interest The authors declare that they have no conflict of interest.

Ethical approval This study does not contain any studies with human or animal subjects performed by any of the authors.

References

1. Kashyap AK, Pandey A (2018) Different nature-inspired techniques applied for motion planning of wheeled robot: a critical review. Int J Adv Robot Autom 3(2):1–10
2. Lever JH, Denton D, Phetteplace GE et al (2006) Mobility of a lightweight tracked robot over deep snow. J Terramech 43(4):527–551. https://doi.org/10.1016/j.jterra.2005.09.002
3. Hildebrand M (1959) Motions of the running cheetah and horse. J Mammal 40(4):481–495. https://doi.org/10.2307/1376265
4. Park J, Kim KS, Kim S (2014) Design of a cat-inspired robotic leg for fast running. Adv Robot 28(23):1587–1598. https://doi.org/10.1080/01691864.2014.968617
5. Di Carlo J, Wensing PM, Katz B et al (2018) Dynamic locomotion in the MIT cheetah 3 through convex model-predictive control. In: 2018 IEEE/RSJ International Conference on Intelligent Robots and Systems, p.1–9 https://doi.org/10.1109/IROS.2018.8594448
6. Semini C, Tsagarakis NG, Guglielmino E et al (2010) Design and experimental evaluation of the hydraulically actuated prototype leg of the HyQ robot. In: 2010 IEEE/RSJ International Conference on Intelligent Robots and Systems, p.3640–3645. https://doi.org/10.1109/IROS.2010.5651548
7. Nelson G, Saunders A, Playter R (2019) The PETMAN and Atlas robots at Boston Dynamics. In: Goswami A, Vadakkepat P (Eds.), Humanoid Robotics: a Reference. Springer, Dordrecht, p.169–186. https://doi.org/10.1007/978-94-007-6046-2_15
8. Zhang K, Zhang JH, Gan MY et al (2022) Modeling and parameter sensitivity analysis of valve-controlled helical hydraulic rotary actuator system. Chin J Mech Eng 35(1):66. https://doi.org/10.1186/s10033-022-00737-w
9. Barasuol V, Villarreal-Magaña OA, Sangiah D et al (2018) Highly-integrated hydraulic smart actuators and smart manifolds for high-bandwidth force control. Front Robot AI 5:51. https://doi.org/10.3389/frobt.2018.00051
10. Kim JT, San Cho J, Park BY et al (2013) Experimental investigation on the design of leg for a hydraulic actuated quadruped robot. IEEE ISR 2013:1–5. https://doi.org/10.1109/ISR.2013.6695685
11. He J, Gao F (2020) Mechanism, actuation, perception, and control of highly dynamic multilegged robots: a review. Chin J Mech Eng 33(5):120–149. https://doi.org/10.1186/s10033-020-00485-9
12. Xu B, Zong HZ, Zhang JH et al (2022) Research status and development trend of carbon fiber reinforced polymer hydraulic cylinder. Acta Materiae Compositae Sinica 39(2):446–459 (in Chinese). https://doi.org/10.13801/j.cnki.fhclxb.20210824.002
13. Türk DA, Triebe L, Meboldt M (2016) Combining additive manufacturing with advanced composites for highly integrated robotic structures. Procedia CIRP 50:402–407. https://doi.org/10.1016/j.procir.2016.04.202
14. Gao J, Xiao M, Zhang Y et al (2020) A comprehensive review of isogeometric topology optimization: methods, applications and prospects. Chin J Mech Eng 33(1):87. https://doi.org/10.1186/s10033-020-00503-w
15. Shi G, Guan C, Quan D et al (2020) An aerospace bracket designed by thermo-elastic topology optimization and manufactured by additive manufacturing. Chin J Aeronaut 33(4):1252–1259. https://doi.org/10.1016/j.cja.2019.09.006
16. Yang JK, Gu DD, Lin KJ et al (2022) Laser additive manufacturing of bio-inspired metallic structures. Chin J Mech Eng Addit Manuf Front 1(1):100013. https://doi.org/10.1016/j.cjmeam.2022.100013
17. Huang H, Zhang JH, Xu B et al (2021) Topology optimization design of a lightweight integrated manifold with low pressure loss in a hydraulic quadruped robot actuator. Mech Sci 12(1):249–257. https://doi.org/10.5194/ms-12-249-2021
18. Wang JR, Xi YX, Ji C et al (2022) A biomimetic robot crawling bidirectionally with load inspired by rock-climbing fish. J Zhejiang Univ Sci A (Appl Phys & Eng) 23(1):14–26. https://doi.org/10.1631/jzus.A2100280
19. Bai XJ, Shang JZ, Luo ZR et al (2022) Development of amphibious biomimetic robots. J Zhejiang Univ Sci A (Appl Phys & Eng) 23(3):157–187. https://doi.org/10.1631/jzus.A2100137
20. Heglund NC, Taylor CR (1988) Speed, stride frequency and energy cost per stride: how do they change with body size and gait? J Exp Biol 138(1):301–318. https://doi.org/10.1242/jeb.138.1.301
21. Wang YJ, Liu CB, Ren LQ et al (2022) Bioinspired soft actuators with highly ordered skeletal muscle structures. Bio-Des Manuf 5(1):174–188. https://doi.org/10.1007/s42242-021-00148-1
22. Zhang JH, Huang H, Liu G et al (2021) Stiffness and energy absorption of additive manufactured hybrid lattice structures. Virtual Phys Prototyp 16(4):428–443. https://doi.org/10.1080/17452759.2021.1954405
23. Zhang M, Lin RC, Wang X et al (2020) 3D printing of Haversian bone–mimicking scaffolds for multicellular delivery in bone regeneration. Sci Adv 6(12):86725. https://doi.org/10.1126/sciadv.aaz6725
24. Bigham A, Foroughi F, Rezvani Ghomi E et al (2020) The journey of multifunctional bone scaffolds fabricated from traditional toward modern techniques. Bio-Des Manuf 3(4):281–306. https://doi.org/10.1007/s42242-020-00094-4
25. Zhang SS, Li HM, Huang YC (2021) An improved multi-objective topology optimization model based on SIMP method for continuum structures including self-weight. Struct Multidiscip Opt 63(1):211–230. https://doi.org/10.1007/s00158-020-02685-2